The [S II] velocity map of Fig. 18a confirms these trends even more, with slightly positive velocities being found also to S-E of NGC 6530 cluster core, almost parallel to the Great Rift. The positive-velocity datapoints in this region follow closely the inner border of the bright-rimmed dark cloud hosting the massive protostar M 8E-IR, while velocities just outside the bright rim (i.e., projected against the most obscured part) become suddenly negative. Again, the sharpest velocity gradients occur along a line joining M 8E-IR with the Hourglass region (arrow in Fig. 16), so that a more detailed understanding can be achieved from considering position-velocity diagrams along this direction. Before doing that, however, we consider the spatial maps obtained from results of the 2-g fits.

A 2-g velocity map for [N II] is shown in Fig. 18b. We preferred to study this line with respect to the brighter Hα because the narrower line widths permit a better determination of individual component velocities. We have omitted the weakest components, which contribute more to the noise than to show a clear pattern. The most important features shown are the crowdings of positive-velocity datapoints near M 8E-IR and along a vertical strip passing through 9 Sgr and Hourglass. Also indicated are the positions of the sub-mm knots found by Tothill et al. (2002; they did not explore the northern half of the nebula): the orange datapoints fill almost exactly the arc-shaped region delimited to the south by those knots, and ending with M 8E-IR to the east. Also the orange datapoints in the Hourglass region tend to fill the interior of a region delimited by the sub-mm knots to the south. Almost everywhere else, no receding component (with respect to $RV_{\rm cm}$) is observed in the ionized gas, even considering the 2-g line profile models.

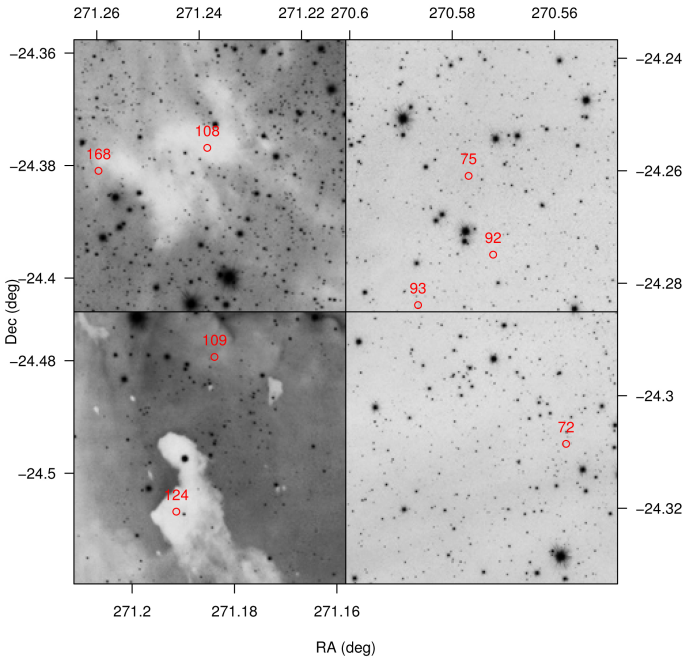

Fig. 19. Examples of dark globules projected against bright background (*left*), and the extreme west of the nebula. Sky fibre positions (only) are indicated, for some of which spectra are shown in Fig. 4 and discussed in the text.

3.3.1. Peculiar locations

The image of the nebula shows several dark globules or "elephant trunks" projected against the bright nebular background. For some of these dark nebulae we have fibre spectra, enabling us to discriminate the properties of the foreground gas against that of the brighter background. Two such examples are shown in Fig. 19, left panels. The one in the lower left panel (called the Dragon by Brand & Zealey 1978; and Tothill et al. 2008) is one of the most evident, and its spectrum was shown in Fig. 4, labeled as Nr. 124. This latter reveals that the nebular emission, although attenuated by a factor ∼10 with respect to adjacent unobscured positions, is still substantial, and images show it as dark only because of the sharp contrast with the surrounding bright emission; nevertheless, this spectrum shows a peculiar component, as a significant emission residual at velocity ∼−50 km s^{-1}. This is not seen, at least not as clearly as here, in any other spectrum, including those of other obscured patches like that in the upper left panel of Fig. 19. Therefore, at least in the direction of the Dragon, we see that ionized gas with velocity ∼−50 km s^{-1} exists above a distance from the nebula enclosing ∼90% of the bulk emission, from simple aperture photometry with respect to nearby unobscured positions. The existence of faster gas component at large distances agrees with the results from the sodium lines presented in Sect. 3.2, and with those of Meaburn (1971) on [O III] lines.

The right panels of Fig. 19 show instead the locations, in the extreme west of the entire nebula, where the most asymmetric or even splitted line profiles are found in our dataset (spectra labeled as Nr. 72, 92, 93 both here and in Fig. 4); here again the nebular emission is so weak as to appear nonexistent in the narrow-band image, but is enough to be detected and studied in our spectra. Figures 4 and 19 together show that the nebular line profiles vary smoothly with spatial position, which confirms that their peculiarities do not arise from some random effect, or isolated cloudlet. We will discuss therefore the implied large-scale motion of this part of the nebula in Sect. 3.4.3.

3.3.2. The position of 9 Sgr

Another peculiar location is that of the most massive star, 9 Sgr, which as mentioned is suspected to lie at some distance (5–10 pc according to Lada et al. 1976) in front of the cloud. Assuming like these authors that it is the dominant ionizing source for the entire nebula (i.e., except in the vicinity of Herschel 36 or HD 165052), its line-of-sight distance from the nebula may actually be estimated from the decay of measured ionization with sky-projected distance. We are able to estimate the ionization parameter q from the Hα/[N II] ratio, using for example the curves shown by Viironen et al. (2007), and the electron density $N_{\rm e}$ from the [S II] doublet ratio. The product $qN_{\rm e}$ is proportional to ionizing flux F; this will follow a spatial decay like $F = I_0/(r^2 + d_{\rm rad}^2)$, where r is the sky projected distance from 9 Sgr, and $d_{\rm rad}$ is the line-of-sight distance of 9 Sgr from the nebula, assumed flat. Figure 20 shows the result of this experiment: a well defined peak is indeed found, with additional, local enhancements in ionizing flux near +3 and −20 arcmin due to Herschel 36 and HD 165052, respectively; a minor enhancement near −9 arcmin corresponds instead to the B stars in the NGC 6530 core. The proposed functional form for F is shown by the lines, with the green one corresponding to 3 arcmin, or $d_{\rm rad}$ = 1.09 pc at the nebula distance. If the adopted curve maximum is lowered, to account for the fact that the actual maximum in the datapoints is due to Herschel 36, a 4-arcmin curve is also satisfactory, corresponding to $d_{\rm rad}$ = 1.46 pc. These normal distances are much smaller than the estimates by Lada et al. (1976); one possible explanation is the assumed planar geometry for the illuminated nebula: a slightly convex geometry would increase center-to-edge differences, and require larger $d_{\rm rad}$ to produce the

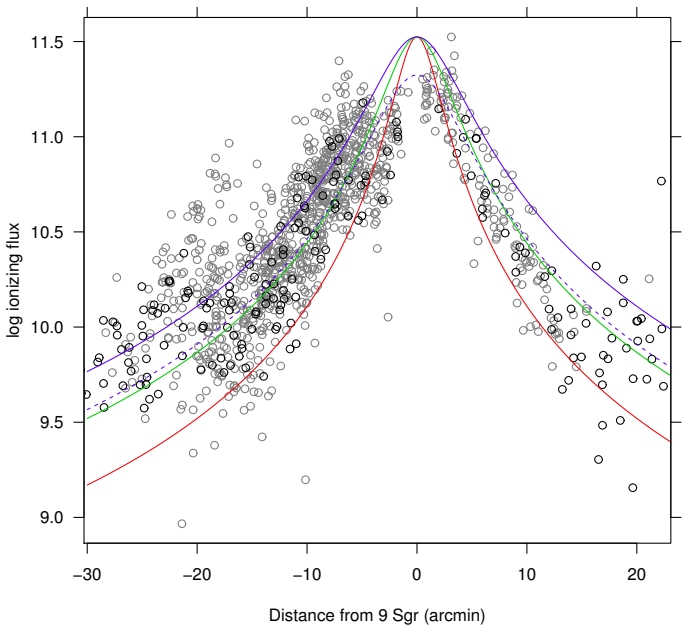

Fig. 20. Ionizing flux vs. radial distance from 9 Sgr, shown separately for the eastward and westward directions (negative and positive distances, respectively). Black (gray) dots refer to pure-sky (faint star) fibres. The blue, green, and red solid lines refer to normal distances of 1.46, 1.09, and 0.73 pc, respectively. The blue dashed line refers to a distance of 1.46 pc, adopting a different maximum flux.

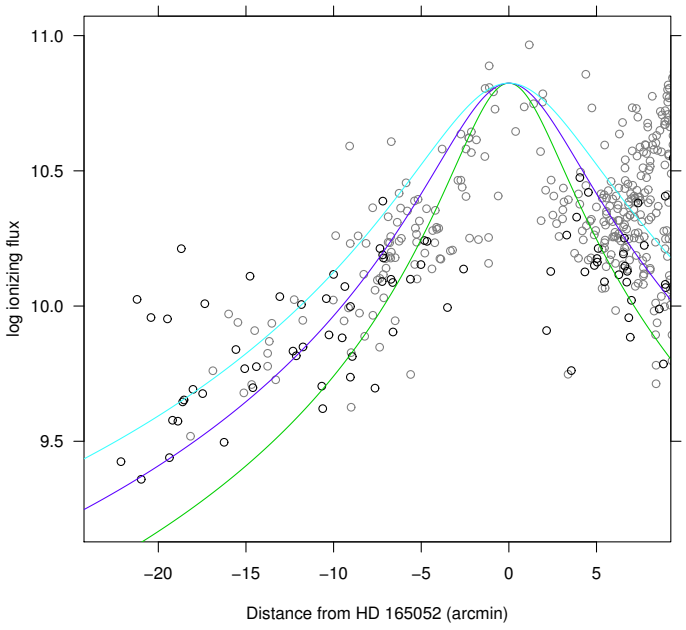

Fig. 21. Ionizing flux vs. radial distance from HD 165052, shown separately for the eastward and westward directions. Symbols as in Fig. 20. Cyan, blue, and green, solid lines refer to normal distances of 1.82, 1.46, and 1.09 pc, respectively.

same observed effect. However, lacking these detailed geometrical informations on the nebula itself, we cannot derive better estimates, and may only consider $d_{\rm rad}$ = 1.09–1.46 pc as lower limits to the 9 Sgr distance from the part of the nebula immediately behind it.

This distance is much larger than the distance between the Orion-nebula ionizing star θ^1 Ori C and its molecular cloud, of ~0.25 pc (Wen & O'Dell 1995; O'Dell 2001). This difference is undoubtedly an important factor and may explain many of the differences we find between the properties of M 8 and the Orion nebula (see Sect. 3.4.1). It also suggests that 9 Sgr has excavated a larger cavity in its parent cloud compared to θ^1 Ori C, and in turn than the M 8 H_{II} region as a whole is probably in a later evolutionary stage than the Orion nebula.

Both Figs. 20 and 15a suggest that HD 165052 (O7Vz+O7.5Vz binary, Arias et al. 2002) is instead the dominant ionizing source in its neighborhood, despite being almost irrelevant to the nebular dynamics (Figs. 16 and 17). This is confirmed by the dependence of ionizing flux from distance to this star, shown in Fig. 21, analogous of Fig. 20; five arcmin to the west of HD 165052, the flux from 9 Sgr still dominates, but nearer to HD 165052 the 9 Sgr contribution becomes unimportant. We can therefore fit (although with higher uncertainties) a profile depending on the normal distance from HD 165052 to the cloud, as above: it turned out that also this star, like 9 Sgr, is likely to be found distinctly above the cloud, at a distance in the range 1.5–1.8 pc.

3.4. Position-velocity diagrams

3.4.1. The NGC 6530 region

Having discussed in Sect. 3.3 the existence of a reference direction for the nebular velocity field (arrow in Fig. 16), we study here position-velocity diagrams along this direction. This symmetry properties pertaining only to the region around the NGC 6530 cluster core, we consider here only the region (24 arcmin in diameter) within the red circle in Fig. 16. The relevant position-velocity diagram for Hα (with velocities from 1-g fits) is shown in Fig. 22. Positive projected distances are toward the arrow head of Fig. 16, that is toward the galactic plane (to N-W). The origin of distances is at the reference position of the NGC 6530 core, shown in Fig. 16. As mentioned, the low-mass cluster stars have a well-defined peak in their RV distribution, at $RV_{\rm cm}$ = 0.5 ± 0.2 km s^{-1} (Prisinzano et al. 2007); it is reasonable to assume that also the B stars in the same spatial region have the same mean RV. The most massive star in the cluster core region is HD 164906 (MWC280; type B0Ve, Levenhagen & Leister 2006). The cluster center coincides also with a CO bright spot (nr. 3 in Lada et al. 1976), at velocity $RV \sim +6$ km s^{-1} (heliocentric, corresponding to $v_{\rm LSR} \sim 16$ km s^{-1} as reported in Lada et al.), whose position is also shown in Fig. 17. As Fig. 22 shows, the cluster core corresponds to the expansion center, in both position and velocity, of a shell-like structure in the ionized gas, reaching maximum negative speeds of ~−12 km s^{-1}; no gas is found at $RV \sim RV_{\rm cm}$ in the vicinity of the cluster center. Interestingly, the colder CO molecular gas moves in the opposite direction with respect to $RV_{\rm cm}$, and Fig. 4 of Lada et al. (1976) also shows that it possesses a velocity gradient along the N-S direction, suggesting a shell-like geometry as well. The resulting picture is that of a localized expanding gaseous bubble, pushed by the cumulative effect of winds from massive B stars in the NGC 6530 cluster core (there are no O stars inside it). Therefore, in this part of the Lagoon nebula the nebular emission arises in front of the star cluster, not in its background. As the velocity map of Fig. 16 shows, such expansion is not spherical, with near-zero radial velocity reached at small distances only along the direction of the arrow. While dust extinction in front of the cluster stars is relatively low, it rises considerably behind them (e.g., Damiani et al. 2006), implying large amounts of dust just behind the cluster. Interestingly, there is no trace in Fig. 22 of any receding ionized shell, which we interpret with the ionizing radiation

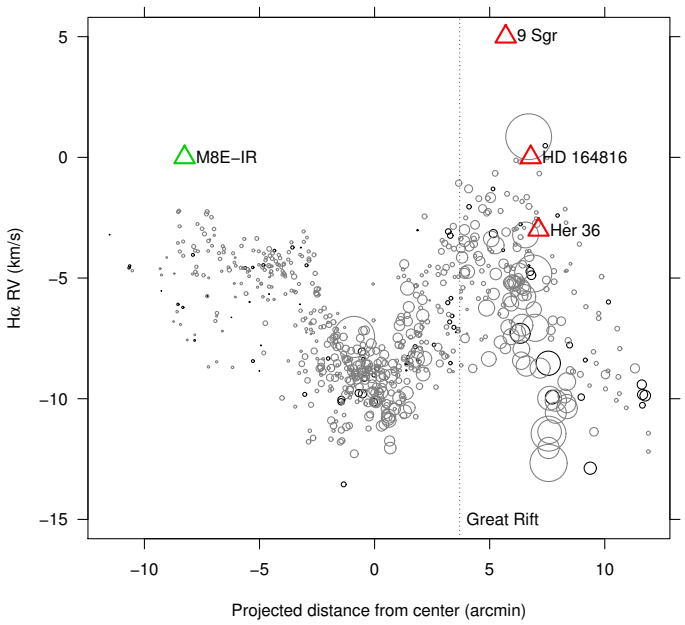

Fig. 22. Position-velocity diagram for Hα, inside the cluster core region (red dashed circle in Fig. 16). The projected distances in the abscissae are computed along the direction of the arrow also shown in Fig. 16. RVs from 1-g fits. Symbol size is proportional to line intensity from 1-g fits. Black (gray) circles refer to pure-sky (faint-star) fibres. The O star HD 164816 and the massive object M 8E-IR (triangles), for which no RV measurements are available, are plotted at $RV = 0$, that is the NGC 6530 cluster velocity, while the other triangles indicate massive-star RVs as reported in Table 1.

being absorbed by the dust on the rear side. For comparison, in the Orion nebula a rather regular sequence of velocities is found, with some of the ionized gas layers having speeds within a few km s^{-1} relative to the background CO ($\Delta RV \sim 3$ km s^{-1} for [S II], ~ 7 km s^{-1} for [O III], $\sim$10 km s^{-1} for Hα; O'Dell et al. 1993; O'Dell 2001). Here instead (and see also Fig. 26 below) we see little or no ionized gas at velocities so close to that of background CO, which points to important differences between the structure of the ionized regions in M 8 and in the Orion nebula. Also the emission from the PDR on the molecular cloud surface is not clearly recognizable in the position-velocity diagrams.

The stellar wind push of the massive stars in the NGC 6530 core, on the other hand, may be responsible for the peculiar positive-velocity displacement of the CO emitting gas (we note that the other two CO spots found by Lada et al. 1976, the brightest one coincident with the Hourglass nebula, have velocities $\sim$0 km s^{-1}, heliocentric). The current view that the star cluster did form on the near-side surface of the molecular cloud is in good agreement with the proposed interpretation: the far side of the star cluster faces regions with more dust, molecular gas, and higher-density gas in general, than the near side, facing the outer, more rarefied parts of the cloud. Therefore, also the absolute speed reached by the near-side ionized diffuse gas (~-12 km s^{-1} in Hα) is larger than than of the far-side denser and colder gas ($\sim+6$ km s^{-1} in CO).

At projected distances larger than +5 arcmin, Fig. 22 shows a wide scatter in the RV distribution, with no clearly defined geometry; this region corresponds to the Hourglass nebula, as also clear from the size of the symbols in the figure (proportional to intensity). In the figure are also shown the massive stars M 8E-IR, HD 164816, 9 Sgr, and Herschel 36. Interpreting such a complex velocity field in term of expansion driven by one or more massive stars requires to know the radial velocity of these stars with sufficient accuracy. This information is not always available for massive stars, which have few lines broadened by very fast rotation, are found very often in binary systems, and are studied mostly with single-epoch observations. For convenience we compiled in Table 1 the literature radial-velocity data on the most massive stars discussed here, from the SIMBAD database, except for the 9 Sgr velocity taken from Williams et al. (2011); we note however that this star is a long-period SB2 binary, and the systemic velocity is subject to large errors (Rauw et al. 2012). No *Gaia*-ESO velocity measurements are available for these massive stars. Literature velocities are missing for four stars, including the massive young object M 8E-IR. These are plotted in our position-velocity diagrams at a velocity $RV_{\rm cm}$ for reference. The two stars in the western regions have similar velocities (~-10 km s^{-1}), but strongly discrepant with $RV_{\rm cm}$; yet, they agree more with the approaching velocity of the Hα emission in the same region, discussed in Sect. 3.4.3 below. The positive velocity of 9 Sgr is surprising at first sight, being so different from that of the CO clouds; however, after considering that this star lies $\sim$1.5 pc above a massive molecular cloud ($2–6\times10^4$ $M_\odot$ for each of the CO clouds in the region according to Takeuchi et al. 2010, with the cloud associated with the Hourglass being one of the most massive), it becomes plausible that this star has gained a considerable speed toward the cloud during the last few Myrs.

From Fig. 22 there is no apparent connection between the position and motion of 9 Sgr and the ionized gas, despite this star being the most massive of the region. This supports further the arguments of Lada et al. (1976) on its lying at some distance from the cloud, in its foreground. In those outermost nebular regions, the local gas density is likely so low that the ionized front approaching us becomes undetectable. Outside the ionized regions, there is nevertheless neutral gas associated with the Lagoon nebula, as discussed in connection with sodium absorption in Sect. 3.2. Therefore, Fig. 23 shows the same Hα velocities as in Fig. 22, but on an expanded velocity scale, with the addition of the Na I D velocities: except for the dominant component near -5 km s^{-1}, the neutral gas moves at much larger negative velocities than the Hα-emitting gas. No clear pattern is seen, indicating that the geometry of the neutral-gas expansion is different from that of the ionized gas. It is interesting to remark that despite 9 Sgr is distant from the nebula, the sodium absorption is still closer to us, since several absorption components at negative velocities up to ~-25 km s^{-1} or more are evident also in the 9 Sgr UVES spectra shown in Fig. 24. In this Figure a definite time variability of the sodium absorption components is seen, especially near velocities ~-20 km s^{-1}, in both velocity and line width; this agrees with our arguments of Sect. 3.2 that the sodium layer at ~-20 km s^{-1} is the one most subject to dynamical changes.

Consideration of the 2-g model fits to the Hα line in the same cluster core region provides us with only a marginally clearer picture (Fig. 25): the velocity splitting between blue and red components is here mostly small compared to the absolute velocity values. Again, near the shell center essentially no near-zero-velocity gas is detected, while maximum negative velocities attain ~-15 km s^{-1}. In the Hourglass region the velocity spread is highest, again without clear geometrical pattern; we recall that this latter property agrees with the highly anisotropic brightness distribution of the Hourglass nebula itself, whose obscuring material lets the radiation from Herschel 36 leak only through irregularly-distributed windows.

Table 1. Literature data for massive stars in the Lagoon nebula.

Name	RA J2000	Dec J2000	Spectral type	RV km s^{-1}
HD 164536	270.6609	–24.2554	O7.5V	–10.5
7 Sgr	270.7129	–24.2825	F2/F3II/III	–11.1
Herschel 36	270.9180	–24.3785	O7:V	–3.0
9 Sgr	270.9685	–24.3607	O4V((f))z	5.0
HD 164816	270.9869	–24.3126	O9.5V+B0V	
HD 164865	271.0634	–24.1834	B9Iab	
M 8E-IR	271.2244	–24.4448		
HD 165052	271.2940	–24.3986	O7V+O7.5V	1.2
HD 165246	271.5195	–24.1955	O8V	

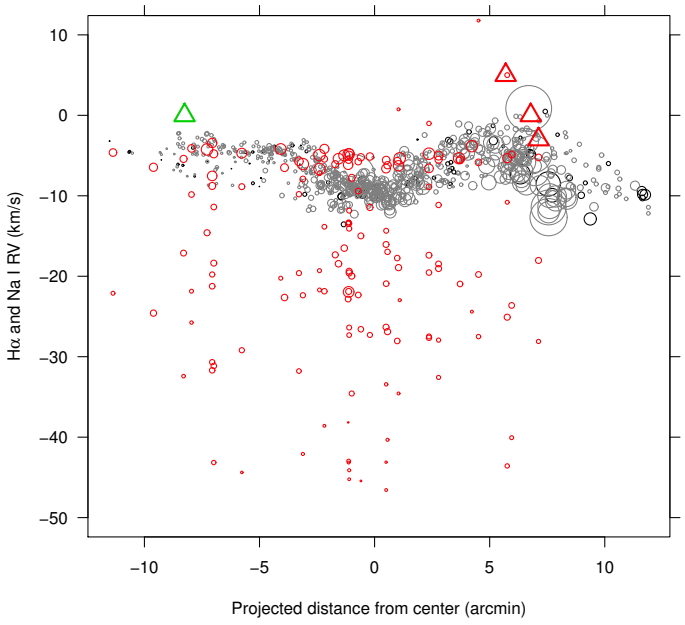

Fig. 23. The same diagram as in Fig. 22, but on a wider RV range to show also the Na I D2 absorption velocities (red circles).

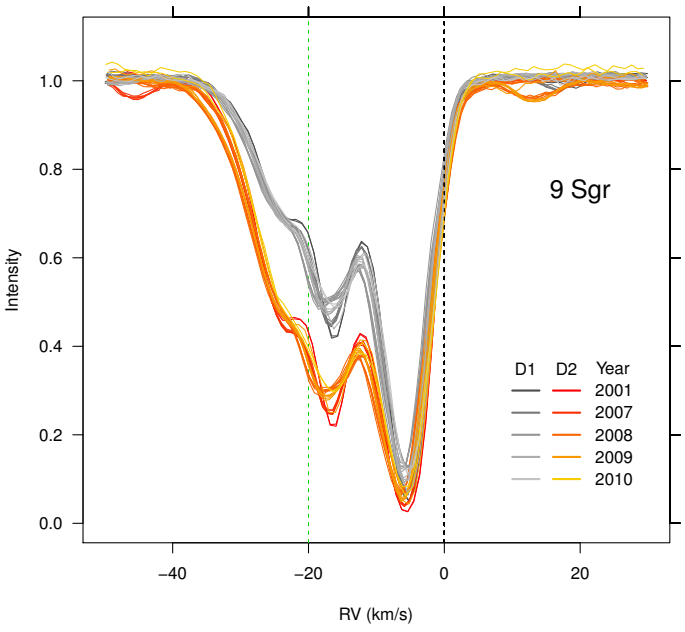

Fig. 24. Sodium doublet absorption toward 9 Sgr from UVES spectra between 2001–2010. Velocity $RV = -20$ km s^{-1}, where significant line-profile changes are found, is marked with a green dashed line.

More illuminating is the examination of the position-velocity diagram involving 2-g fits to [N II] and [O III] lines, and shown in Fig. 26. While the emission at velocities between 0 to −10 km s^{-1} has not greatly changed, new features are seen at both positive velocities (as in the map of Fig. 18b), and at velocities <−10 km s^{-1}. In the projected distance range from ∼−10 to ∼−3 arcmin a weak but significant positive-velocity component is found in both [N II] and [O III]. The velocity is found to be largest near the projected position of M 8E-IR (green triangle), and to decrease gradually toward position ∼−3 arcmin. There is no corresponding structure in the position-velocity plane at negative velocity. This suggests strongly the existence of a shell of ionized gas, expanding away from M 8E-IR (or its immediate vicinity), of which only the receding component is visible to us, and limitedly to the part unobscured by the dense bright-rimmed cloud. This latter characteristics is easily explained assuming that any approaching gas is blocked or hidden by the dark dusty structures seen as bright-rimmed clouds, which also occult M 8E-IR from our direct view. While all the literature on this object (see the review in Tothill et al. 2008) agrees that it must be very young and surrounded by thick layers of dust, the existence of a hemispheric shell ionized by this object implies that the dust thickness between M 8E-IR and the nebula behind it is much less than the dust thickness in the direction toward us. Alternatively, M 8E-IR, a known outflow source (Mitchell et al. 1991), might be only the source of the mechanical push exerted on the receding gas, which is instead ionized by another UV source, maybe 9 Sgr further away. Even in this latter case, the total column density of matter on our side of M 8E-IR must be much larger than on its rear side, in order to block any approaching gas expanding from it.

Considering now the region around 9 Sgr ($RV = +5$ km s^{-1}, Fig. 26), we observe that positive-velocity emission is found near its position, up to $RV \sim +12$ km s^{-1}, and declining away from the star position. Already in Fig. 18a the positive-velocity datapoints were seen to follow an almost half-arch around this star's position. While no (or very little) positive-velocity gas is found in correspondence of the cluster core, blocked by the dense molecular material behind, this blocking effect does not operate for the gas receding from 9 Sgr, if this star lies at large distances in front of the cluster as already discussed. Therefore, we obtain a coherent picture by assuming that the positive-velocity gas is pushed by 9 Sgr toward the nebula, counteracting its expansion locally.

The region around the Hourglass and Herschel 36 continues to show a rather chaotic position-velocity pattern even using the 2-g model fits in Fig. 26 as it was using 1-g models in Fig. 22 above. The largest green circle in Fig. 26 represents the strong negative-velocity [O III] emission in the Herschel 36 spectrum; a corresponding, much weaker positive-velocity component is also found near ∼+8.5 km s^{-1}, demonstrating again asymmetric expansion in the immediate vicinity of this star, where the high-ionization [O III] line arises.

Finally, Fig. 26 shows, in correspondence to cluster core, the largest negative velocities (up to ∼−25 km s^{-1}), which overlap with the velocities of the sodium absorption where indications of a hotter absorbing gas were found, as discussed in Sect. 3.2.

3.4.2. The Hourglass nebula

We next discuss position-velocity diagrams in the Hourglass region (defined as in Fig. 16); since the positive-velocity datapoints align along approximately the N-S direction in Fig. 18a, we take here the reference direction along RA for the position axis. The position-velocity diagram of Fig. 27 shows together

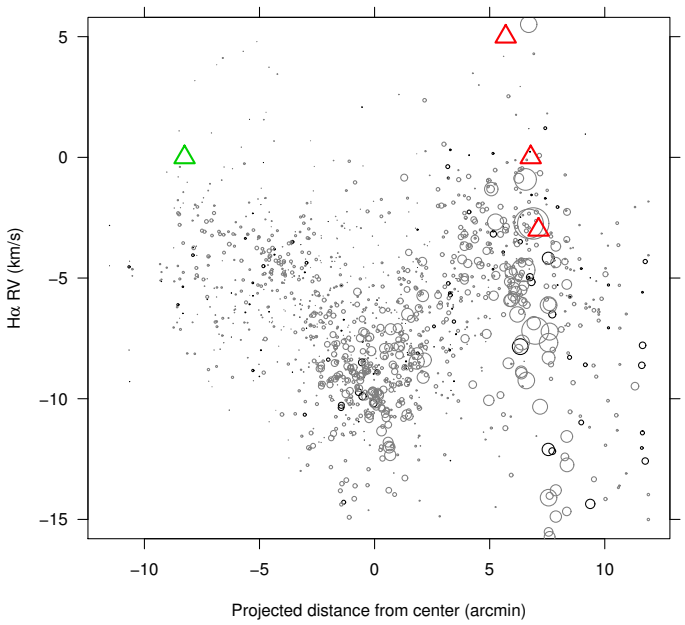

Fig. 25. Position-velocity diagram for Hα, cluster core, with RVs from 2-g fits. Symbol meaning as in Fig. 22.

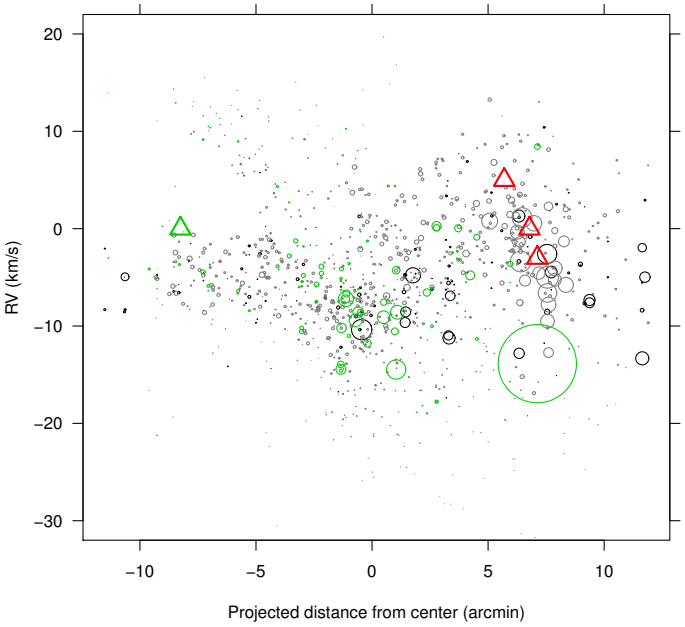

Fig. 26. Position-velocity diagram for [N II], cluster core, from 2-g fits. Also shown with green circles are the best-fit [O III] components.

the 2-g fit results from four lines: [N II], Hα, [O III], and Na I absorption. The position origin is taken coincident with the RA of 9 Sgr (RV = +5 km s^{-1}). Herschel 36 lies at RV = −3 km s^{-1}. The diagram, although very complex, helps us to appreciate better several effects. The [N II] emission, although found at both positive and negative velocities in the neighborhood of 9 Sgr, is on average stronger at positive RVs, whereas Hα is largely absent at positive RVs. This explains the discrepancy of bulk velocities between the two lines, found in Fig. 5a. To the right of position origin, the velocity splitting in Hα increases regularly until the position of Herschel 36: there, Hα shows both a negative-velocity component (reaching ∼−18 km s^{-1}), and a slower component, apparently at rest with respect to Herschel 36. On the other hand, [N II] shows both a rest-frame

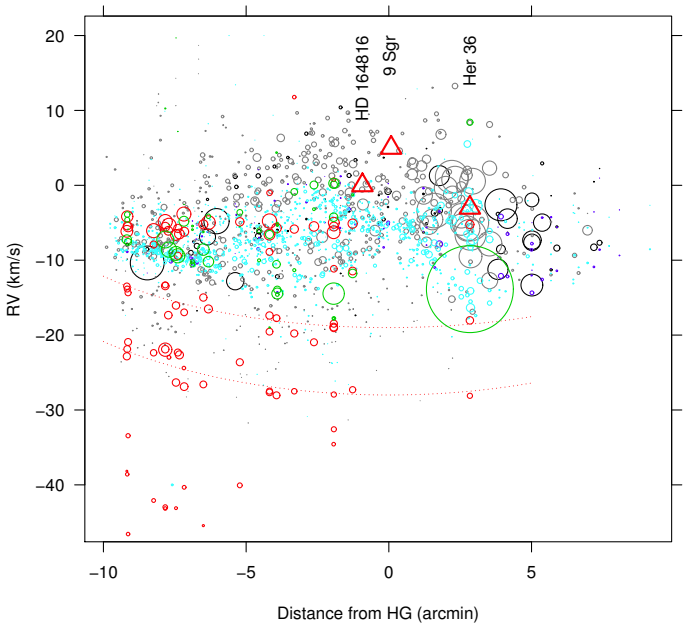

Fig. 27. Position-velocity diagram, in the Hourglass region (orange dashed circles in Fig. 16), showing RVs from 2-g fits. Circle size is proportional to line intensity. Positions in the abscissae are along RA direction, from the reference point shown in Fig. 16. Black and gray circles refer to [N II] (sky fibres and faint stars as in Fig. 22), blue and cyan circles refer to Hα, green circles to [O III], and red circles to Na I absorption. The large dotted circle segments are visually fit to the sodium datapoints.

component and another one with slightly receding velocities with respect to Herschel 36. Also in this case as for 9 Sgr, the Hα to [N II] intensity ratio is different between the near and far side of the massive star. We cannot make more quantitative studies since the intensity ratios for the (unresolved) 2-g fit components are affected by too large errors individually, as remarked in Sect. 3.1. The existence of positive-velocity [N II] emission from the envelope around Herschel 36, unlike the cluster core region, suggests that this star like 9 Sgr lies at some distance above the dust-rich molecular cloud, otherwise an inward-directed flow at positive velocities would have been blocked.

Much fainter than the positive-velocity [N II] emission, but still clearly detected is negative-velocity [N II] at ∼−20 km s^{-1}, overlapping some of the Na I absorption layers. As also discussed in Sect. 3.2, the transition between ionized and neutral gas should take place near this velocity range. Although the spatial coverage of the UVES data used for the study of the sodium line is much less dense than that of the Giraffe data, we may tentatively identify in the figure a regular pattern in the sodium absorption, as indicated by the two dotted red curves. These are centered to the 9 Sgr position, and suggest that the large-scale expansion, at distances where the gas is neutral, is driven by this star. The radii of the circle segments shown in Fig. 27 are respectively 13 and 15 arcmin, corresponding to 4.74 and 5.47 pc. The star 9 Sgr, showing sodium absorption at least around −20 km s^{-1}, must be interior to at least the lower-velocity shell, in agreement with its line-of-sight position derived in Sect. 3.3.2. By dividing the inferred sodium-shell radii by their maximum velocities we obtain timescales of order of 2–2.5 × 10^5 yr. Note however that even stars farther away from 9 Sgr than 15 arcmin show sodium absorption, so that the proposed geometry for the absorbing layers must be only considered as tentative, and more complex neutral-gas structures are

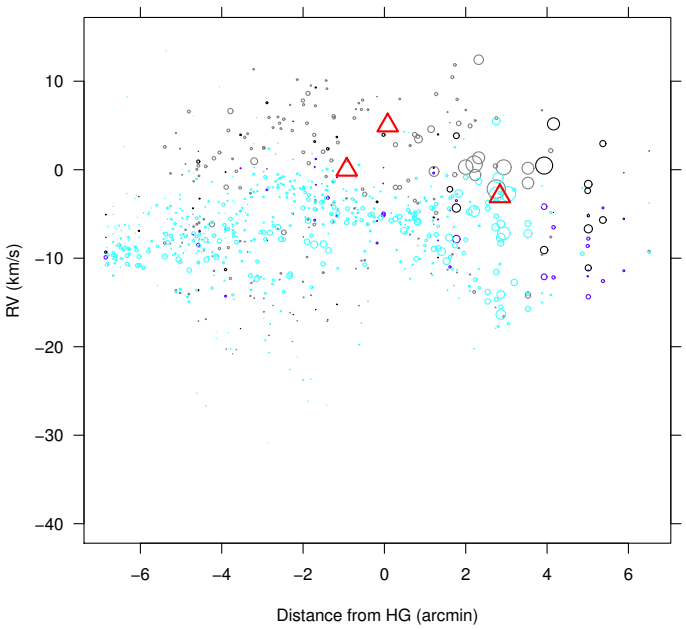

Fig. 28. Analogous of Fig. 27, but showing RVs from 2-g fits to [S II] (gray and black) and Hα (cyan and blue).

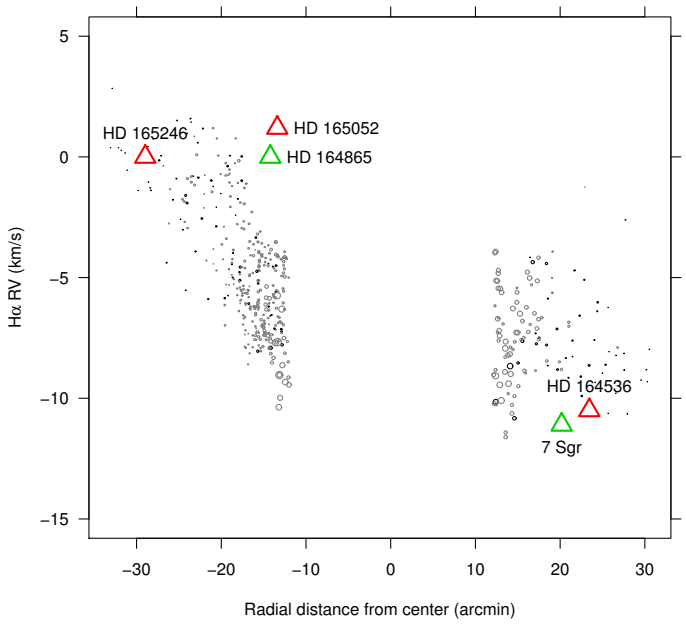

Fig. 29. Large-scale RV dependence on radius, from Hα (1-g fits). Only datapoints external to the cluster-core region (red dashed circle in Fig. 16) are shown. The abscissae show radial distances from cluster center (red plus sign in Fig. 16), shown separately for the eastern (left) and western (right) parts. Symbols as in Fig. 22.

certainly present across the entire face of the nebula. These layers, well above the ionized gas, and at negative velocities with respect to it, are very similar to the Orion Veil, already mentioned in Sect. 3.1. The existence of a blueshifted, neutral layer is also in very good agreement with predictions of champagne-flow models of blister H_{II} regions (Tenorio-Tagle 1979), fully appropriate to a region like M 8.

The results from the 2-g fits to [S II] lines, shown in Fig. 28, provide independent confirmations of the findings just discussed. In particular the brightest [S II] emission near Herschel 36 is found near the stellar rest velocity (as for Hα), but clear [S II] emission near the Hourglass is found also at positive velocities (while Hα shows large negative velocities in the same region).

3.4.3. The outer parts of the Lagoon nebula

Finally, we examined the large-scale velocity patterns of the nebula, outside the central parts examined above. We have already remarked that the western regions do not show the same dynamics as the eastern ones, and therefore a radial coordinate does not prove useful. Instead, we consider separately an east and a west radial coordinate, from the same NGC 6530 cluster center as in Sect. 3.4.1. The dependence of 1-g Hα velocity on these radial distances is shown in Fig. 29. Toward east the gradual decrease in absolute velocity (toward RV_{cm}) agrees well with a global-expansion pattern, with velocity vectors becoming orthogonal to the line of sight at the largest radii. To the west, there is no sign of this, with velocities remaining at values from -10 to -5 km s^{-1} even where the nebula becomes very faint. Our spatial sampling in the S-W outer regions is almost nonexistent, so these result pertain essentially to the N-W parts, that is those closest to the galactic plane. Adding complexity to the puzzle, the two massive stars in the west (HD 164536 and 7 Sgr) both have negative velocities, similar to the neighboring gas but contrasting with RV_{cm}.

One possible explanation of the east-west large-scale velocity gradient in the Lagoon is rotation. In order to keep in bound keplerian rotation matter at a speed of 5 km s^{-1} at a radius of 10-11 pc, and in the absence of internal pressure support, a mass of 6×10^4 $M_\odot$ is required, which is not unreasonable compared to the mass estimates for the CO clouds in M 8 given by Takeuchi et al. (2010) using NANTEN, or the value of 10^4 $M_\odot$ given for the M 8-East region alone by Tothill et al. (2008). However, one obvious difficulty of this hypothesis is that, if this was the case, then Fig. 29 would suggest for the cloud center of mass a $RV \sim -5$ km s^{-1}, in strong disagreement with the RVs of both the CO bright spots of Lada et al. (1976) and the NGC 6530 RV_{cm}.

The adoption of 2-g fits does not clarify the issue of large-scale dynamics, even using [N II] and [O III] having smaller linewidths (Fig. 30): not only the datapoint scatter is increased, but the overall east-west velocity gradient becomes barely observable in these lines, which therefore originate in layers well distinct from Hα. For some locations, as discussed in Sect. 3.3.1, the [N II] lines are split, with central RV very close to that of the nearby O star HD 164536: these add to the scatter seen in the rightmost datapoints in Fig. 30, where local expansion adds to the average local cloud velocity. The splitting center being so close to the O-star RV might also be seen as a confirmation that the (poorly studied) star HD 164536 lies within the Lagoon itself. The figure also shows velocities of sodium absorption components, which may be of some usefulness: if we consider the lowest-found (absolute) sodium velocities at various radial distances, we may observe a regular gradient from $RV \sim 0$ km s^{-1} at the east extreme, toward $RV \sim -5$ km s^{-1} at the opposite one. As discussed in Sect. 3.2, this sodium layer, being the most uniform of all found here, is probably the outermost one, and therefore least affected by local phenomena. If it is really associated with the Lagoon nebula, it might be considered as the best indicator of a global rotation of the nebula. A much better spatial coverage in the sodium absorption data would be needed, however, before accepting this possibility.

Alternatively, the observed velocity gradient might reflect a shear motion, caused by interaction between the parts of M 8

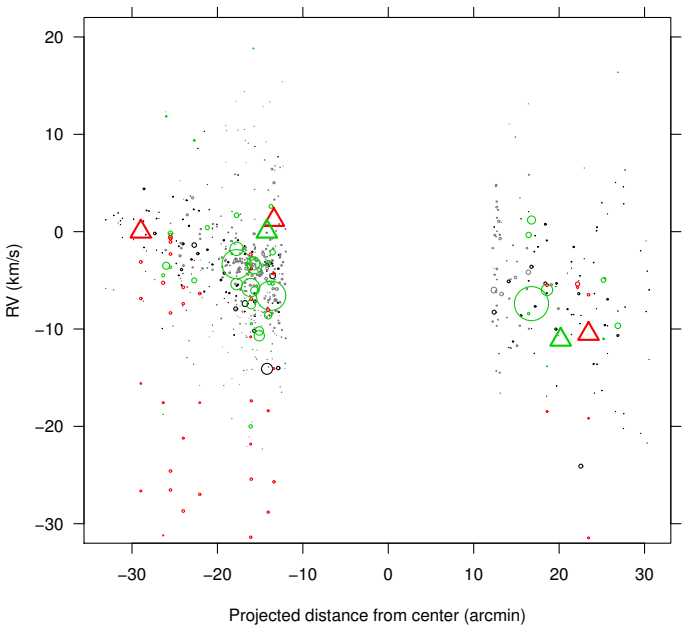

Fig. 30. Same as Fig. 29, but showing RVs from 2-g fits to [N II] (black and gray) and [O III] (green). Also shown are RVs of Na I absorption (red).

closest to the galactic plane (to the northwest) and other dense clouds.

4. Discussion and summary

The various pieces of evidence described in Sect. 3 enable us to draw a complex picture of the ionized and neutral gas in the Lagoon nebula, and of its physical connection to massive stars and molecular material in the cloud. Perhaps the most effective way of building a coherent and understandable picture is by means of a drawing. We show therefore a graphical summary of most of the results obtained in Fig. 31, which refers to a section through the nebula along a line joining M 8E-IR with the Hourglass region, until the western nebula parts. The figure represents most of our findings with some level of detail. It shows the approximate boundary of the molecular cloud, dusty regions, and some O stars as a reference.

The core of the NGC 6530 cluster is shown, where most of its B stars are found; the entire cluster would fill most of the region shown. The B stars drive a strong expanding shell toward us visible in the ionized-gas lines. On the opposite (far) side of the cluster, no redshifted expansion is detected in the ionized lines, suggesting that the cluster lies very close to the denser, dusty molecular cloud, as shown. The CO clump in the same direction is redshifted (Lada et al. 1976; Takeuchi et al. 2010), probably pushed by the same cluster stars producing the blueshifted optical lines. We represent this with the magenta dashed arcs. Note that the other two strong CO clumps in this region (also labeled "CO" in the figure) are found at rest with respect to the NGC 6530 $RV_{\rm cm}$.

The Hourglass region around Herschel 36 lies probably at some distance from the background molecular cloud, since some high-velocity redshifted emission is seen around it, as well as blueshifted emission. The geometry of any material expanding away from Herschel 36 is however very irregular, because of the non-isotropic distribution of dense clouds all around this star: we represent this as discontinuous shell fragments, both redshifted and blueshifted. We recall that the nebular densities found in this region are the highest of the whole Lagoon nebula.

The M 8-East region is also characterized by a partial-shell geometry, since we detect the unobscured portion of a redshifted expanding arc, centered on M 8E-IR. This star, or another sufficiently massive star near to it, must be heavily obscured on our side (tens of magnitudes visually), but very little on the inner side, in order to be able to drive an inward flow. The outward flow is instead blocked by the dense cloud, and its blueshifted emission not detected accordingly.

A crucial role is played by the most massive star, 9 Sgr, which we find to lie well separated (at least 1 pc, or more) from the cloud surface, in agreement with previous works, but still inside the large blister concavity. Being found in a low-density environment, its radiative and mechanical push becomes detectable only against the higher-density gas on the inward side of the star, as redshifted emission in [N II] and [S II]; on its outward side, very faint or undetectable blueshifted emission is present. A combination of factors may therefore explain the characteristics found in the Great Rift region: it is denser than its surroundings, being compressed by both sides (NGC 6530 shell and Herschel 36 shell), and pushed toward the cloud by the 9 Sgr wind and radiation, hence the positive velocities on its ionized surface. It would be interesting to examine whether such compression is able to trigger new star formation. There is no contradiction between the enhanced dust density in the Great Rift, responsible for obscuration of background stars, and the inconspicuous electron density found there from the [S II] doublet ratio (Fig. 15b), since this latter only refers to its ionized surface and not to its colder, inner parts.

Completing the picture, the western parts of the cloud are found to be approaching us, as is the O star HD 164536, whose wind is probably responsible of some line splitting in its vicinity, indicative of a bidirectional expansion, as shown. At large distances in front of the whole cloud, discrete neutral layers are found, approaching us over a range of (negative) velocities and distances. They might be named the "Lagoon Veil", by analogy with the Orion Veil.

In addition to these results, at least another one deserves some discussion. The velocity profile around NGC 6530, whatever the diagnostic line and the modeling approach (1-g or 2-g) chosen, leaves little doubt about an expanding shell being driven by stars in the cluster core. At the same time, both the ionization parameter (Fig. 15a) and the ionizing flux (Fig. 20) show a gradient across the cluster face, in the direction of 9 Sgr. The latter figure shows that, with respect to the 9 Sgr ionizing flux, only a small excess (less than a factor of 2) is found at the NGC 6530 position, attributable to the NGC 6530 B stars themselves. Therefore we reach the conclusion, on solid observational grounds, that the NGC 6530 shell is mechanically driven from inside, but ionized from outside. This geometry is very unlike classical Strömgren spheres. A deeper treatment of the problem is clearly outside our scopes here. The biggest problem is, since we observe recombination in the Hα line, where the recombined neutral gas lies: gas outside of the shell is ionized by 9 Sgr, inside it is ionized by the NGC 6530 B stars. Perhaps a double shell develops, with an intermediate sheet of neutral gas: this might account for the small velocity splitting indicated by our 2-g fits to Hα lines. In the absence of a detailed modeling, we cannot however derive any firm conclusion on this issue.

Another interesting issue is that related to rotation of the entire cloud, as suggested by the blueshifted lines in the N-W parts. It is worth noting in this respect that in the molecular CO lines the appearance of the Lagoon nebula is very different than in

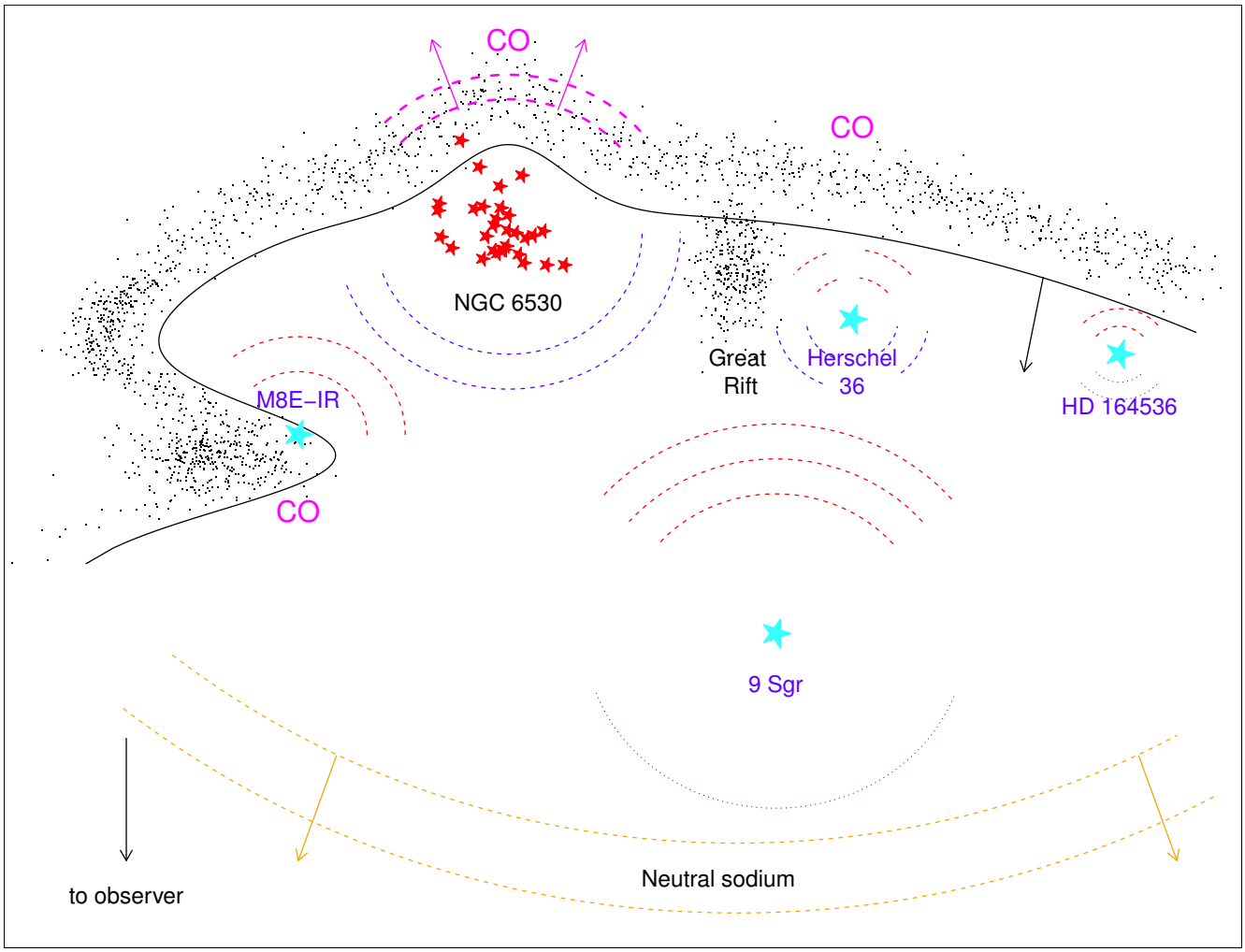

Fig. 31. Schematic representation of the Lagoon nebula geometry, along a direction passing through M 8E-IR and the Hourglass nebula. The black line indicates the molecular cloud boundary. Dusty regions are indicated with dots. Red (blue) dashed arcs indicate redshifted (blueshifted) ionized gas. Triple arcs indicate more conspicuous emission, single arcs weak emission; broken arcs indicate irregular shells. The position and motion of the known CO clouds is indicated in magenta. The most massive stars and the NGC 6530 cluster core are indicated with cyan and red stars respectively. The large-scale sodium layers are also shown (yellow dashed lines), probably not to scale.

the optical, and splits in three main condensations, coincident with M 8-East, NGC 6530 core, and Hourglass regions respectively, with little in between (Fig. 8 of Takeuchi et al. 2010). The Lagoon N-W regions appear as an extension of the Hourglass CO cloud, whose core is at rest with respect to $RV_{\rm cm}$. It is therefore possible that only the Hourglass molecular cloud is rotating, not the entire Lagoon nebula; this motion does not involve NGC 6530 and is in better agreement with the other existing dynamical data. Alternatively, the CO maps of Takeuchi et al. (2010) make it clear that the N-W region, the closest to the galactic plane, is also near other CO clouds, and might be interacting with them. Therefore, while the bulk motion of approach of the N-W Lagoon nebula region is an established observational result, its interpretation is not unambiguous.

Acknowledgements. We wish to thank an anonymous referee for his/her many interesting comments and suggestions. Based on data products from observations made with ESO Telescopes at the La Silla Paranal Observatory under program ID 188.B-3002. These data products have been processed by the Cambridge Astronomy Survey Unit (CASU) at the Institute of Astronomy, University of Cambridge, and by the FLAMES-UVES reduction team at INAF-Osservatorio Astrofisico di Arcetri. These data have been obtained from the *Gaia*-ESO Survey Data Archive, prepared and hosted by the Wide Field Astronomy Unit, Institute for Astronomy, University of Edinburgh, which is funded by the UK Science and Technology Facilities Council. This work was partly supported by the European Union FP7 program through ERC grant number 320360 and by the Leverhulme Trust through grant RPG-2012-541. We acknowledge the support from INAF and Ministero dell' Istruzione, dell' Università' e della Ricerca (MIUR) in the form of the grant "Premiale VLT 2012". T.Z. acknowledges support from the Slovenian Research Agency (research core funding No. P1-0188). F.J.-E. acknowledges financial support from the Spacetec-CM project (S2013/ICE-2822). M.T.C. acknowledges the financial support from the Spanish Ministerio de Economía y Competitividad, through grant AYA2016-75931-C2-1-P. The results presented here benefit from discussions held during the *Gaia*-ESO workshops and conferences supported by the ESF (European Science Foundation) through the GREAT Research Network Programme. This work is also based on data products from observations made with ESO Telescopes at the La Silla Paranal Observatory under program ID 177.D-3023, as part of the VST Photometric Hα Survey of the Southern Galactic Plane and Bulge (VPHAS+, www.vphas.eu). This research has made use of the SIMBAD database, operated at CDS, Strasbourg, France.

References

Arias, J. I., Morrell, N. I., Barbá, R. H., et al. 2002, MNRAS, 333, 202
Bagnulo, S., Jehin, E., Ledoux, C., et al. 2003, The Messenger, 114, 10
Balick, B., Gammon, R. H., & Hjellming, R. M. 1974, PASP, 86, 616
Bohuski, T. J. 1973, ApJ, 184, 93
Brand, P. W. J. L., & Zealey, W. J. 1978, A&A, 63, 345
Damiani, F., Flaccomio, E., Micela, G., et al. 2004, ApJ, 608, 781
Damiani, F., Prisinzano, L., Micela, G., & Sciortino, S. 2006, A&A, 459, 477
Damiani, F., Bonito, R., Magrini, L., et al. 2016, A&A, 591, A74

Drew, J. E., Gonzalez-Solares, E., Greimel, R., et al. 2014, MNRAS, 440, 2036
Elliott, K. H., & Meaburn, J. 1975, MNRAS, 172, 427
Gilmore, G., Randich, S., Asplund, M., et al. 2012, The Messenger, 147, 25
Henning, T., & Gürtler, J. 1986, Ap&SS, 128, 199
Hobbs, L. M. 1974, ApJ, 191, 381
Kaufman, U., & Martin, W. C. 1993, J. Phys. Conf. Ser., 22, 279
Kramida, A., Ralchenko, Yu., Reader, J., & NIST ASD Team 2015, NIST Atomic Spectra Database (v. 5.3), http://physics.nist.gov/asd
Kumar, D. L., & Anandarao, B. G. 2010, MNRAS, 407, 1170
Lada, C. J., Gottlieb, C. A., Gottlieb, E. W., & Gull, T. R. 1976, ApJ, 203, 159
Levenhagen, R. S., & Leister, N. V. 2006, MNRAS, 371, 252
Meaburn, J. 1971, Ap&SS, 13, 110
Mitchell, G. F., Maillard, J.-P., & Hasegawa, T. I. 1991, ApJ, 371, 342
Munari, U., & Zwitter, T. 1997, A&A, 318, 269
O'dell, C. R. 2001, ARA&A, 39, 99
O'dell, C. R., Valk, J. H., Wen, Z., & Meyer, D. M. 1993, ApJ, 403, 678
O'Dell, C. R., Muench, A., Smith, N., & Zapata, L. 2008, Handbook of Star Forming Regions, Vol. I, ed. B. Reipurth (ASP Monograph Publications), 4, 544
Pasquini, L., Avila, G., Blecha, A., et al. 2002, The Messenger, 110, 1
Povich, M. S., Kuhn, M. A., Getman, K. V., et al. 2013, ApJS, 209, 31
Prisinzano, L., Damiani, F., Micela, G., & Sciortino, S. 2005, A&A, 430, 941
Prisinzano, L., Damiani, F., Micela, G., & Pillitteri, I. 2007, A&A, 462, 123
Randich, S., Gilmore, G., & Gaia-ESO Consortium 2013, The Messenger, 154, 47
Rauw, G., Sana, H., Spano, M., et al. 2012, A&A, 542, A95
Saraph, H. E., & Seaton, M. J. 1970, MNRAS, 148, 367
Simon, M., Cassar, L., Felli, M., et al. 1984, ApJ, 278, 170
Sung, H., Chun, M.-Y., & Bessell, M. S. 2000, AJ, 120, 333
Takeuchi, T., Yamamoto, H., Torii, K., et al. 2010, PASJ, 62, 557
Tenorio-Tagle, G. 1979, A&A, 71, 59
Tothill, N. F. H., White, G. J., Matthews, H. E., et al. 2002, ApJ, 580, 285
Tothill, N. F. H., Gagné, M., Stecklum, B., & Kenworthy, M. A. 2008, Handbook of Star Forming Regions, Vol. II, ed. B. Reipurth (ASP Monograph Publications), 5, 533
van den Ancker, M. E., The, P. S., Feinstein, A., et al. 1997, A&AS, 123, 63
Viironen, K., Delgado-Inglada, G., Mampaso, A., Magrini, L., & Corradi, R. L. M. 2007, MNRAS, 381, 1719
Walker, M. F. 1957, ApJ, 125, 636
Weedman, D. W. 1968, PASP, 80, 314
Welsh, B. Y. 1983, MNRAS, 204, 1203
Wen, Z., & O'dell, C. R. 1995, ApJ, 438, 784
Williams, S. J., Gies, D. R., Hillwig, T. C., McSwain, M. V., & Huang, W. 2011, AJ, 142, 146
Woodward, C. E., Pipher, J. L., Helfer, H. L., et al. 1986, AJ, 91, 870
Wright, E. L., Lada, C. J., Fazio, G. G., Low, F. J., & Kleinmann, D. E. 1977, AJ, 82, 132

Appendix A: Additional tables

Table A.1. Fitting results (1-g models) for nebular emission lines.

Id	RA	Dec	Hα			[N II] 6584			[S II] 6717			[S II] 6731		
	(J2000)		RV	σ	Norm	RV	σ	Norm	RV	σ	Norm	RV	σ	Norm
SKY_18041349-2406277	271.0562	-24.10769	–4.44	13.33	13604.47	–3.32	9.82	5303.02	–2.45	9.49	893.61	–2.19	9.48	653.69
SKY_18040836-2411076	271.0348	–24.18544	–8.67	13.35	71283.37	–5.89	13.05	10866.23	–3.70	12.88	2182.28	–3.58	12.71	1608.08
SKY_18041039-2413163	271.0433	–24.22119	–2.41	13.35	44833.48	2.03	10.90	6861.96	2.98	10.89	1360.72	2.84	10.59	997.84
SKY_18043822-2413504	271.1592	–24.23067	–7.78	14.11	32206.53	–4.93	11.19	6559.79	–4.35	11.04	1178.57	–4.06	10.83	856.31
SKY_18043552-2406457	271.1480	–24.11269	–5.75	13.88	8302.00	–4.48	10.82	3030.67	–4.37	10.60	661.15	–4.14	10.58	478.39
SKY_18043039-2411382	271.1266	–24.19394	–7.91	13.73	45666.66	–4.08	11.60	10108.42	–2.68	11.34	1992.34	–2.49	11.19	1479.74
SKY_18044986-2410494	271.2077	–24.18039	–6.08	13.54	24539.49	–3.82	11.38	8360.59	–1.76	11.49	1839.73	–1.83	11.10	1320.87
SKY_18042865-2415336	271.1194	–24.25933	–8.52	13.18	44827.42	–5.82	10.46	7341.40	–4.70	10.00	1366.45	–4.62	9.83	1034.42
SKY_18043273-2417261	271.1364	–24.29058	–8.83	13.68	16638.05	–4.96	11.79	2305.00	–4.53	11.39	531.72	–4.47	10.64	388.39
SKY_18045577-2415459	271.2324	–24.26275	–7.12	14.10	21283.13	–4.00	12.58	6772.99	–4.41	12.38	1149.48	–4.32	12.05	821.87
SKY_18043471-2416492	271.1446	–24.28033	–8.51	13.62	46025.05	–5.27	11.36	5759.30	–3.64	11.00	1221.82	–3.59	10.72	925.07
SKY_18050209-2410250	271.2587	–24.17361	–5.00	14.01	11658.67	–3.08	11.63	4058.60	–2.10	11.18	937.26	–1.71	11.51	690.53
SKY_18050407-2417194	271.2670	–24.28872	–6.59	14.11	6440.37	–5.05	11.84	1703.00	–4.56	11.63	396.81	–4.29	11.64	290.20
SKY_18043741-2418209	271.1559	–24.30581	–9.02	14.09	53120.50	–7.15	12.93	7183.70	–5.76	12.30	1375.30	–5.75	11.92	1008.91
SKY_18042325-2423135	271.0969	–24.38708	–9.76	13.04	92195.82	–9.26	12.77	10544.73	–6.68	12.47	2340.38	–6.23	12.22	1782.30
SKY_18042233-2424399	271.0930	–24.41108	–10.13	13.35	81644.76	–9.24	12.86	12434.13	–8.79	12.66	2410.94	–8.44	12.43	1806.04
SKY_18035290-2419527	270.9704	–24.33131	–4.73	13.29	103114.41	–0.16	11.45	15344.15	1.19	11.42	2948.04	1.59	11.08	2451.45
SKY_18040022-2416517	271.0009	–24.28103	0.48	14.22	58118.20	8.01	12.99	7824.35	6.78	14.20	1210.24	6.85	13.96	917.58
SKY_18034573-2418216	270.9405	–24.30600	–9.93	13.65	84000.85	–3.75	10.69	18035.57	–2.44	10.97	3429.26	–2.19	10.65	2984.15
SKY_18030577-2416564	270.7740	–24.28233	–7.74	13.96	27976.36	–6.61	11.41	8938.61	–6.18	11.04	1992.20	–5.86	11.16	1526.26

Notes. Units of RV and σ columns are km s^{-1}. Units of Norm columns are ADU km/sec/min. Full table available at the CDS.

Table A.2. Fitting results for Na I D2 lines.

Id	Name	v_1 (km s^{-1})	σ_1 (km s^{-1})	N_1 (km s^{-1})	v_2 (km s^{-1})	σ_2 (km s^{-1})	N_2 (km s^{-1})	v_3 (km s^{-1})	σ_3 (km s^{-1})	N_3 (km s^{-1})	v_4 (km s^{-1})	σ_4 (km s^{-1})	N_4 (km s^{-1})	v_5 (km s^{-1})	σ_5 (km s^{-1})	N_5 (km s^{-1})
580-1	18040126-2423474	–5.01	1.48	208.52	–11.14	10.10	6.69	–18.47	2.20	10.29	–27.94	5.63	2.13			
580-2	18041116-2421452	–1.01	8.68	2.66	–4.77	1.23	3071.49	–17.38	3.36	11.62	–27.48	3.75	4.28			
580-3	18042056-2424556	–4.98	1.13	2029.78	–16.51	7.44	20.68									
580-4	18042433-2415168	–3.84	1.01	2523.49	–24.40	2.57	0.55									
580-5	18042502-2427453	–6.50	3.00	80.45	–22.64	4.72	21.36									
580-6	18042663-2419321	–5.34	1.12	2811.36	–22.97	1.52	0.66									
580-7	18042720-2422497	–4.84	1.06	2667.80	–13.44	7.88	14.49	–21.95	0.57	1435.09	–43.16	1.04	0.55			
580-8	18043893-2424142	–4.19	1.27	1458.15	–20.24	3.10	1.66									
580-9	18044279-2418339	–4.75	1.26	455.51	–14.07	3.00	5.41	–19.38	1.73	12.75	–26.37	2.66	4.45	–45.23	3.00	0.48
580-10	18044593-2427191	–4.24	1.24	3100.19	–14.59	8.59	13.68									
580-11	18045062-2425419	–3.43	1.46	338.62	–8.78	3.19	35.49	–21.24	9.12	8.65	–30.68	1.26	6.12			
580-12	18045273-2417525	–4.94	1.14	2850.68	–19.30	3.54	1.74									
580-14	18053923-2407522	–5.25	1.75	157.38	–17.57	3.92	4.92	–31.20	2.53	0.52						
580-16	18055648-2416004	–0.59	2.72	965.69	–0.74	7.46	27.64	–24.58	2.41	35.00	–41.33	0.21	0.14			
520-1	18023863-2415195	–6.48	2.33	27.77	–19.17	2.70	2.83	–31.45	3.79	6.19						
520-2	18024192-2433360	–5.38	1.03	2573.53	–5.72	3.00	12.44									
520-3	18025328-2420170	–5.50	2.11	38.28	–18.47	4.37	5.14	–33.29	2.22	4.39						
520-4	18033016-2430506	–5.33	0.97	2438.88	–5.58	3.00	13.45									
520-5	18034033-2422427	–5.23	2.98	24.67	–18.03	5.00	12.82	–28.11	5.00	2.10						
520-6	18035837-2429128	–5.12	1.61	54.09	–11.45	4.54	16.17	–27.30	3.87	4.89						

Notes. Column Id is the Setup+star identifier used in Sect. 3.2. Column Name is based on J2000 star coordinates. Units of N_i are the same as σ_i by Eq. (3). Full table available at the CDS.